LAWRENCE
LIVERMORE
NATIONAL
LABORATORY

LLNL-JRNL-608092

Exploring high temperature phenomena related to post-detonation by an electric arc

Z. Dai, J. C. Crowhurst, C. D. Grant, K. B. Knight, V. Tang, E. G. Cook, J. P. Lotscher, I. D. Hutcheon

December 13, 2012

Journal of Applied Physics

Disclaimer

Exploring high temperature phenomena related to post-detonation using an electric arc

Z. R. Dai,[a] J. C. Crowhurst, C. D. Grant, K. B. Knight, V. Tang, A. A. Chernov, E. G. Cook, J. P. Lotscher, and I. D. Hutcheon

Lawrence Livermore National Laboratory, Livermore, California 94551-0808, USA

We report a study of materials recovered from a uranium-containing plasma generated by an electric arc. The device used to generate the arc is capable of sustaining temperatures of an eV or higher for up to $100\,\mu s$. Samples took the form of a $4\,\mu m$-thick ^{238}U film deposited onto 8 pairs of $17\,\mu m$-thick Cu electrodes supported on a $25\,\mu m$-thick Kapton backing and sandwiched between glass plates. Materials recovered from the glass plates and around the electrode tips after passage of an arc were characterized using scanning and transmission electron microscopy. Recovered materials included a variety of crystalline compounds (e.g., UO_2, UC_2, UCu_5,) as well as mixtures of uranium and amorphous glass. Most of the materials collected on the glass plates took the form of spherules having a wide range of diameters from tens of nanometers to tens of micrometers. The composition and size of the spherules depended on location, indicating different chemical and physical environments. A theoretical analysis we have carried out suggests that the submicron spherules presumably formed by deposition during the arc

[a] Author to whom correspondence should be addressed. Electronic mail: dai1@llnl.gov.

discharge, while at the same time the glass plates were strongly heated due to absorption of plasma radiation mainly by islands of deposited metals (Cu, U). The surface temperature of the glass plates is expected to have risen to ~2,300 K thus producing a liquefied glass layer, likely diffusions of the deposited metals on the hot glass surface and into this layer were accompanied by chemical reactions that gave rise to the observed materials. These results, together with the compact scale and relatively low cost, suggest that the experimental technique provides a practical approach to investigate the complex physical and chemical processes that occur when actinide-containing material interacts with the environment at high temperature, for example, during fallout formation following a nuclear detonation.

I. INTRODUCTION

Nuclear forensics is an emerging science benefitting from the application of advanced analytical techniques and an improved understanding of the physico-chemical processes associated with a nuclear detonation.[1, 2] Fallout is material formed from a cooling fireball following a detonation, in which unburned fuel, structural materials, and associated fission and activation products are incorporated with surrounding environmental material such as water, dust and soil.[3] Fallout may capture chemical, physical and isotopic evidence reflecting the physical conditions and chemical environment associated with a detonation.[3] Beginning with Adams et al.,[4] studies of the composition, structure and origin of radioactive fallout debris have been an area of active investigation. Only ~10% of all fission products are estimated to be transported from the fireball and incorporated into soil as fallout and only a small component of fallout and related debris contains material associated with the device (fuel, fission products, activation and stable products from casing and structural components).[5] The formation and preservation of complex debris at the micron- and sub-micron scale has been demonstrated,[2, 4] as well as predicted on a theoretical basis.[6-8]

Despite years of empirical studies, many fundamental questions relating to the physics of fireball dynamics and the formation of fallout and related debris remain, including an understanding of the linkage between fallout characteristics and the underlying chemical and physical processes. Comprehensive study of the fundamental relationships between single components of fallout debris is required to answer these questions. From an experimental point of view, this approach entails exposing simple combinations of materials to the conditions present in the cooling fireball, followed by a

detailed examination of the recovered materials and comparison with debris from nuclear tests. There are practical limits as to how accurately fireball cooling conditions can be reproduced in the laboratory, at least in terms of time and length. Nevertheless, a simplified experiment may still be used to place bounds on models, which remain to some extent unconstrained and fail to predict or explain the heterogeneous composition, structure and chemical fractionation of fallout materials.[2] In this work we use an electric arc generated by a spark gap to produce a uranium-containing plasma. The plasma is allowed to condense and interact with its surroundings, and recovered materials are then analyzed using scanning electron microscopy, analytical transmission electron microscopy and electron diffraction. The spark gap apparatus is compact and the samples are very small, mitigating safety concerns while permitting rapid throughput. The device is a modified form of a device previously reported by Tang et al[9], allowing extended arc durations from hundreds of ns to ~ 100 μs, while maintaining a temperature near or above 1 eV.

II. EXPERIMENTAL METHODS

A. Spark gap experiment

The spark gap consists of an arrangement of two conducting electrodes separated by an air gap. When the voltage difference between the conductors exceeds the breakdown voltage, a spark or an electric arc forms, ionizing the gas and generating a plasma. The experimental setup used in the present study is similar to that developed by Tang et al.,[9] but the device was modified to generate a much longer lived arc to more closely approximate the cooling conditions of a fireball-generated plasma. In the prior

work, Tang et al. carried out spatial and temporal measurements of the temperature and electron density of the arc-generated plasma and demonstrated that an 1.6-1.7 eV temperature could be achieved, lasting ~570 ns after the start of the discharge, with up to 200 mJ of energy delivered to the arc and a dielectric surface. The experimental system was found to be a useful high-temperature chemistry platform for ablating and heating controlled amounts of solid materials to eV temperatures.[9]

The average temperature of a fireball associated with a nuclear detonation cools from temperatures exceeding ~2 eV (~23,000 K) to below the condensation temperature of most oxides (< 3,000 K) very rapidly, within tenths of seconds to tens of seconds (scaling as a function of yield).[10] To enhance the relevance of the experiments described herein to this cooling regime we added a new "long pulse" pulse-forming network (PFN) to extend the driven plasma duration up to ~140 μs. The PFN is schematically shown in Figure 1 and is made up of modular sections of inductors and capacitors. At charging voltages of 200 V, 2.8 J is stored by the PFN. The PFN is connected to the load in parallel with the "short pulse" pulser and sustains the plasma at ~200 A for ~140 μs after the initial kA arc discharge, lasting 100's of ns.

Figure 2 shows the configuration of the electrodes (Altaflex).[11] The electrodes consist of 17 μm thick, 6.3 mm wide Cu strips with 75 μm wide tips, on a 25 μm thick backing film of Kapton. A window in the Kapton film created a point-to-point breakdown gap of 1 mm (Fig. 2b). Each Kapton sheet or "coupon" contained 8 pairs of electrodes.

Uranium metal films were deposited onto the tips of each electrode pair using magnetron sputtering. Prior to the deposition, the coupon was loaded into the vacuum chamber that was then pumped down overnight to a base pressure of $\leq 8.0\times10^{-8}$ Torr. The

sputtering target was 99.5% pure uranium (^{238}U). Argon was used as the process gas at a controlled flow of 3×10^{-3} Torr at a power of 125 W, which yielded a deposition rate of 90 Å/min.

The final thickness of the uranium film was ~4 μm, other dimensions can be inferred from Fig. 2c. These dimensions were produced using a prefabricated silicon mask during deposition. An error in the relative position of the mask with respect to the electrodes towards the edges of the coupon led to a slight overlap of the uranium onto the Kapton; the deposition closer to the center was more precise (Fig. 2c). After deposition, the coupon was sandwiched between two glass plates and loaded into the arc device. The plates were standard microscope slides (75 mm × 25 mm × 1 mm) made of soda-lime glass and served as substrates for recovering condensed material (Fig. 2a). They also confined the plasma, resulting in a more rapid rate of cooling than observed in unconfined experiments (see Section III-A).

The temperatures of the long pulse arc plasma were measured by time-resolved atomic emission spectroscopy using the Cu atomic emission lines (Cu(I)-510.5 nm, 515.3 nm, 521.8 nm, and 529.3 nm). The data were collected on a laboratory-built confocal system similar to that described previously.[12] The signal was directed into an Andor Technology Inc. Shamrock 303i spectrograph with an electronically gated i-Star-intensified CCD detector. The gate width used in every unconfined experiment was 1 μs. However, the gate width in confined experiments ranged from 0.5 μs to 5 μs depending on the time delay. Details concerning data collection and analysis can be found in Tang et al.[9]

B. Materials characterization

The electrode tips and materials were recovered from the glass substrates and the Kapton backing film after passage of the arc. These materials were characterized using scanning electron microscopy (SEM) and transmission electron microscopy (TEM). SEM analysis was performed using a JEOL 7401-F field emission scanning electron microscope equipped with an Everhart-Thornley secondary-electron detector and a solid state backscattered electron detector for imaging. The SEM is also equipped with an Oxford X-Max (80 mm^2) silicon drift detector and Oxford INCA 250 software to perform X-ray energy dispersive spectroscopy (EDS) measurements of chemical elements.

TEM specimens were prepared using the focused ion beam (FIB) technique,[13] performed under a FEI Nova 600 dual beam microscope. This dual beam microscope is fitted with an Omniprobe *in-situ* micromanipulator and an Ascend Instruments Extreme Access (AIEA) extraction system.

TEM was performed using a Philips CM300-FEG transmission electron microscope with a field emission electron gun operating at 300 kV. The CM300-FEG microscope is equipped with an Oxford X-ray detector for EDS measurements, a Gatan image filter system for energy filtered imaging and electron energy loss spectroscopy (EELS). The instrument can also be used for scanning transmission electron microscopy (STEM) with a probe size ≤ 1.0 nm, and can provide a Z-contrast image, chemical profile and mapping for both X-ray EDS and EELS. Crystal structures were investigated using electron diffraction. Both selected-area electron diffraction (SAED) and electron microdiffraction (μ-diffraction) were employed in the present study. The electron microdiffraction was performed under TEM mode and the beam size is about 10-30 nm.

III. RESULTS AND DISCUSSION

A. Plasma temperature and cooling rate

Figure 3 shows time-resolved plasma temperatures inferred from measured Cu(I) emission lines. In this case pure Cu electrodes were used to generate the arc; the presence of the 4 μm-thick uranium film is expected to have only a minor effect on the plasma temperature. All stated times are relative to the start of the arc as determined from the RLC fit for each individual shot.[9] For the case of plasma confined between glass plates (red-dot data points), the temperature ~5 μs after plasma formation is ~1.32 eV. In the first 80 μs, the temperature drops but remains above 1 eV. The cooling rate then increases and by ~160 μs, the temperature has decayed to 0.74 eV. The temperature decay is due to the cooling and expansion of the plasma.[9] By comparison, the absence of the glass plates (blue-square data points) yields higher temperatures that are maintained at a more constant value of about 1.5 eV for ~100 μs. Although we have not investigated this further, these results suggest a means for controlling the temperature and the cooling rate of the plasma by adjusting the proximity of the substrates to the arc. In these temperature characterizations we have assumed local thermal equilibrium (LTE) between the ion, gas, and electron species, based on prior results using only the fast pulser.[9] These results showed electron densities of ~10^{17}/cm^3 with temperatures of just ~0.5 eV even 15 μs after the main pulse, satisfying Griem's density criteria for LTE.[9] We have not been able to verify LTE, however, because we do not have electron density measurements for these specific plasmas.

B. Characterization of electrodes, pre- and post-arc

The area of uranium film on each of electrode tips was determined using the dimensions shown in Fig. 2c. Nominal thickness of the film is 4 μm. In order to verify the thickness and also to determine phase of the uranium, a cross-sectional TEM sample was prepared using FIB technique. The section was cut at the position marked with a white-line box on the SEM image (Fig. 4a).

Figure 4b is a bright-field TEM image of the cross-section sample. The platinum coating was introduced during TEM sample preparation to protect the sample from ion-beam damage. Beneath the protective coating, the darker uranium and lighter polycrystalline copper can be seen. The uranium exhibits columnar crystalline grains. An approximately 100 nm thick uranium oxide layer can be identified on upper surface of the uranium-metal film, probably the result of post-deposition oxidation in air. The thickness of the uranium metal film was estimated to be ~4 μm, consistent with its nominal deposited thickness.

Metallic uranium has three phases, α, β and γ, which are stable at low-, medium- and high-temperature, respectively.[14, 15] Selected-area electron diffraction patterns taken from the uranium film (Figs. 4c-e) match the α-uranium phase that has an orthorhombic lattice with the space group *Cmcm* (63) and the lattice parameters: a = 2.852 Å, b = 5.865 Å, and c = 4.945 Å.[16] Figures 4f-h are selected-area electron diffraction patterns taken from the copper substrate. All patterns can be indexed as the face-centered cubic (*fcc*) copper crystal ($Fm\bar{3}m$ (225), a = 3.615 Å)[17], as expected.

Figure 5a depicts an electrode tip after an arc. The dashed lines drawn on the image (Fig. 5a) reconstruct the boundaries of original electrode tip, clearly showing that

part of the electrode tip was ablated by the arc. From this reconstruction, we calculate that ~4×10^{-5} *g* (40 μg) of uranium (ρ = 18.97 g/cm^3)[16] and ~8×10^{-5} *g* (80 μg) of copper (ρ = 8.96 g/cm^3)[17] were involved, corresponding to an average composition by mass of 2:1, Cu:U. More than half of this material was deposited onto the unablated parts of the tip next to the ablated section, with the remainder splattered across the confining plates. The spatial distribution of debris was likely influenced by the confining action of the Kapton backing and the glass plate. A few glass fragments were identified in some of the ablated material, visible in Fig. 5a. The morphology of the Kapton backing shows no significant warping or deformity following the passage of the arc, even around the edge of the window (Fig. 5a c.f. Fig. 4a) where the electrode tip existed. Pronounced damage to the surface of the Kapton film is, however, apparent upon close inspection, as discussed in Section III-E.

The bright-field TEM image in Fig. 5b depicts a cross-section cut from the ablated electrode tip at the position indicated by the white-line box in Fig. 5a. Comparison of the image shown in Fig. 5b with that in Fig. 4b reveals that the morphology and structure of the constitutive materials were dramatically altered by passage of the arc. The images indicate that copper and uranium were completely melted and had sufficient time to interact before solidifying. From the base of the image (Fig. 4b), which corresponds to the interior of the electrode, to the top surface where the uranium coating was originally deposited, the post-arc sample displays a layered structure (Fig. 5b). Each layer has a uniform morphology and structure, and variable thickness. EDS spectra indicate that the darker layers, marked as U(Cu) on Fig. 5b, are uranium rich

(>90 wt % U) while the lighter layers, marked as Cu(U) on Fig. 5b, are copper dominant (>50 wt % Cu).

The top-most layer of the post-arc electrode cross-section displays a fine lamellar microstructure. Figure 5c is a Z-contrast dark-field STEM image acquired from a small area of the top layer. As opposed to Fig. 5b, in this dark-field STEM image, the lighter lamellae correspond to higher-Z components. Figure 5d is a selected-area electron diffraction pattern taken from this lamellar structure. The reflections with strong intensities can be indexed to the intermetallic compound UCu_5, a face-centered cubic structure ($F\bar{4}3m$ (216)) with the lattice parameter a = 7.033 to 7.038 Å.[18] The weak satellite reflections around each of the strong reflections can be attributed to copper metal ($Fm\bar{3}m$, a = 3.615 Å)[17] and a multiple scattering effect (e.g., the weak satellite reflections around the transmission spot). Two different orientations of copper crystals are identifiable, forming as a twin in the lamellar structure. X-ray elemental maps (Figs. 5e and 5f) show that this lamellar structure consists of a uranium-rich phase (red) and a copper-rich phase (green), corresponding to the lighter and darker lamellae shown in Fig. 5c, respectively. To summarize, the uranium-rich phase in the lamellar structure is the compound UCu_5, while the copper-rich phase is pure copper metal.

The uranium-copper system was studied by Wilhelm and Carlson,[19, 20] and an equilibrium phase diagram (Fig. 6)[21] was determined on the basis of information obtained by X-ray diffraction, thermal analysis, and metallography. The compound UCu_5 is the only intermediate phase occurring in the uranium-copper binary alloy system. A binary eutectic exists between this compound and copper at the composition of ~75.5 wt% Cu. The eutectic transformation occurs at 950 °C. There is no appreciable solubility of

uranium in copper or, conversely, of copper in uranium. A theoretical study[22] suggested that the solubility of 3*d* transition metals in uranium could be characterized by the electronic structure of the alloys. The insolubility of Cu in uranium may be due to the fully occupied *d*-orbital of Cu. Another distinguishing property of the uranium-copper system is that an almost complete immiscibility exists in the composition region extending from ~1.5 wt % Cu (phase L_1) to ~48 wt % Cu (phase L_2) at temperatures above 1081 °C. This immiscibility was found to hold true even for temperatures of 1,850 °C to 1,900 °C in 25 wt % Cu alloy.[19] The difference in densities of the two liquid phases (L_1 and L_2) can lead to a complete separation in quenching.

As far as composition and structure of the phases are concerned, the lamellar structure of UCu_5 and Cu occurring in the top layer of the post-arc electrode likely formed by the eutectic transformation: $L_2 \rightarrow UCu_5 + Cu$ under thermodynamic equilibrium at 950 °C, i.e., the cooling rate was low enough at the transformation temperature. The U-rich and Cu-rich layers beneath the top layer shown in Fig 5b, are products of quenching of the immiscible liquids L_1 and L_2, which formed before the top layer. This structure implies that an immiscible melt was formed by heating induced by the arc discharge and then solidified rapidly as it contacted the much cooler electrode surface behind the tip. The formation of the eutectic in the top layer can be attributed to a decreased cooling rate, as more material was deposited and perhaps also due to latent heat of solidification. According to the above calculation, however, the average composition of the melted electrode material by mass is about 2:1, Cu:U, a composition located at the single phase zone of L_2 above ~1000 °C in the equilibrium phase diagram (Fig. 6). Immiscibility, therefore, is unexpected under equilibrium conditions and we

infer that heating was not homogenous and the melt did not reach equilibrium in either composition or temperature on the time scale of the arc discharge and subsequent cooling (i.e., hundreds of micro-second (μs)).

C. Materials recovered from confining glass plates

A pair of glass plates was used to capture condensed materials (solid debris), as described above (Fig 2a), following passage of the arc. One plate was located on the same side as the deposited uranium film (the "bottom plate"), in direct contact with the coated electrode. The second plate, located on the opposite side (the "top plate"), was separated from the copper electrodes by a 25 μm-thick Kapton backing. Figures 7a and 8a are low magnification post-arc SEM images of the top and the bottom glass plates, respectively, showing the pattern of debris and the morphology of melt droplets in and around the path of the arc. It is clear that the glass plates sustained significant damage from the passage of the arc. The top plate exhibits a slightly swollen surface and high density of cracks in the region corresponding to the original window in the Kapton film (Fig. 2b). On the bottom plate (Fig. 8a), which was not shielded by Kapton film, the damage is more extensive, extending beyond the boundaries of the window and covering an area twice as large as the window. A large, irregular surface section of glass (darker region) has been ablated, and brittle fractures traverse the exposed underlying glass surface. The ablated glass fragments, indicated by the arrows marked C in Fig. 8a, likely correspond to those found in the melt droplets recovered on the electrodes after an arc (e.g. see Fig. 5a). The plasma likely initiated as a surface discharge across this bottom

plate in direct contact with the electrodes, leading to greater damage on the bottom glass plate.

Fig. 7b shows a magnified image of a damage region from the top plate indicated by arrowhead B on Fig. 7a. A symmetric region of similar damage is clearly visible, indicated by arrowhead A on Fig. 7a. These damage regions display bubbles and/or cavities (dark holes in the inset of Fig. 7b), reflecting heating and degassing of the glass surface. We estimate (in Section III-D) that the temperature of the glass surface may reach to ~2,300 K during the 100 μs arc discharge, comparable with the boiling point of fused silica (SiO_2) glass (2,503 K). The size of the bubbles and cavities varies from sub-micrometer to micrometer scale. Similar damage is also observed on the bottom plate (Fig. 8b) but at locations farther away from center of the window than for the top plate (the regions indicated by the arrows A and B in Fig. 8a), probably indicating closer proximity to and/or higher temperatures in the plasma.

A somewhat different damage pattern can be discerned in Fig. 7c, which shows the region corresponding to arrowhead C of Fig. 7a. This area exhibits craters likely resulting from the impact of material ablated from the electrode tip, to which it was in close proximity. As the arc was triggered, a high-temperature plasma formed between the electrode tips, together with, presumably, a shock wave. The constitutive materials of the electrodes, i.e., copper and uranium, were melted and ejected. Droplets formed in this process were accelerated to high speed by the shock wave and impacted the top plate where the glass was softened or partially liquefied. The high-density melt of copper and uranium was broken into small droplets by the collision and then "splattered" over the plates. Some debris created in these impact events appears to have sufficient energy to

create secondary impact craters, such as those indicated by the white arrowheads in Fig.7c.

In addition to the damage to the confining glass plates, evidence of material redistribution induced by the arc discharge is apparent from the substantial amount of debris deposited on the glass plates over an area corresponding to a circle of ~5 mm diameter centered on the spark gap center. This material appears bright or as light contrast in the SEM images of Fig. 7 and Fig. 8. The majority of the debris on the glass plates occurs in the form of spherules varying in size from tens of nanometers to tens of micrometers, as shown in Figs. 7 and 8. The largest spherule observed on the bottom plate was ~40 μm in diameter (Fig. 8e).

Debris recovered from the top glass plate is shown in Fig. 7. On the basis of EDS analysis, the chemical composition of the spherules varies considerably, with some spherules copper rich and others uranium rich. Shown in the inset of Fig. 7b and the Fig. 7c are backscattered electron SEM images. The micrometer-scale bright spherules in both images all are uranium rich. Abundant sub-micron-scale spherules can also be identified, spread across the imaged area. Chains of spherules indicative of splatter, can be seen in Fig. 7d taken from a region near to the arrowhead C of Fig. 7a.

Debris recovered from the bottom plate (Fig. 8) does not preserve the chains of spherules and splatter-like textures observed on the top plate. The central portion (darker region) that would have been directly exposed to the arc has been completely removed. A "mist" feature can be identified from a low magnification image of the bottom plate (Fig. 8a), covering the surface that was not ablated (e.g., the regions indicated by arrows D and E). Images shown in Figs. 8c (taken near the arrowhead D of Fig. 8a) and 8d (taken from

a flat area indicated by the arrowhead E of Fig. 8a) reveal that the dominant materials are sub-micron spherules ranging from 200 nm to 800 nm in diameter. Each of the sub-micron scale spherules displays a near-perfect spherical shape. Some micrometer scale spherules (>1 μm) also exist, as illustrated in the area shown in Fig. 8c. Path trails and craters can be identified as associated with these larger spherules, as indicated by the solid white arrows (Fig. 8c). Cavities or bubbles are also identified (open arrows in Fig. 8c).

Two sub-micron spherules were choosen for further analysis using TEM. Figures 9a and 9c are bright-field TEM images of cross-sections of the two different spherules, both taken from the bottom glass plate and with similar diameters of ~850 nm. Based on EDS analysis, the spherule shown in Fig. 9a is uranium rich and contains no detectable silicon. In addition, the glass surface under the spherule is flat, implying that no chemical reaction occurred between the spherule and the glass substrate. Electron diffraction analysis reveals that the spherule is crystalline UO_2. One of selected-area electron diffraction patterns is shown in Fig. 9b, which can be indexed as the [110] zone of UO_2 (*fcc*, $Fm\bar{3}m$(225), a = 5.468 Å)[23]. Along with the strong Bragg reflections of the UO_2 crystal, weak diffuse scattering can be identified around the Bragg reflections. The diffuse scattering implies that the UO_2 crystal is not perfect but contains point defects such as oxygen vacancies.

The spherule shown in Fig. 9c is very different from the one described above (Fig. 9a) and is partially embedded into the glass substrate. There is a ~30 nm thick layer (indicated by an arrow) between the spherule and the glass, which we determined by electron diffraction to be composed of ultrafine UO_2 crystallites. The spherule itself

contains only copper and silicon. Figure 9d is a selected-area electron diffraction pattern taken from the spherule. Two types of Cu-Si phases can be identified from the pattern, the ε-Cu_4Si or $Cu_{15}Si_4$ phase (body center cubic (*bcc*) structure, $I\bar{4}3d$ (220), a = 9.694 Å)[24, 25] and the η′′-Cu_3Si phase (tetragonal structure, a = 7.267 Å and c = 7.892 Å).[24] Both phases are intergrowth forming a lamellar microstructure. The streaks occurring on the electron diffraction pattern are associated with the lamellar structure and are caused by plane defects at the boundaries of the phases.

Figure 10 shows the results of TEM measurements on a cross-section of an area similar to that shown in Fig. 8b. The specimen was cut across two dark cavities, as indicated on Fig. 10a. Associated with these cavities, the Z-contrast dark field STEM image (Fig. 10a) and corresponding EDS elemental maps (Figs. 10c and 10d) reveal that uranium mixes into the glass substrate at a depth approaching ~1.5 μm. We infer this mixing reflects diffusion of U and/or chemical reaction between the spherule and the glass. A set of 100-200 nm crystalline particles is embedded in the glass. Electron diffraction analysis (Fig. 10b) identifies these crystalline particles as UO_2. Each embedded UO_2 particle (Fig. 10a) has a euhedral shape different from that of the UO_2 spherules (Fig. 9a) and Cu-Si alloy phases (Fig. 9c), implying a different formation mechanism and/or thermal history. The embedded UO_2 particles should be formed under conditions close to thermal equilibrium.

D. Possible mechanism controlling deposition on glass plates

Here we carry out an analytical effort that attempts to reconstruct the processes leading to formation of the observed products associated with the glass plates (Figs. 7-10).

These processes include propagation of shock waves, transfer of heat, diffusion of gas (air molecules and evaporated Cu/U metal atoms), deposition of metal atoms, and also possible chemical reactions occurring at the glass plates.

The plasma generated by an arc discharge was approximately sustained at the temperature of $T_g = 1.5\times10^4\,\mathrm{K}\,(1.3\,\mathrm{eV})$ for a period of $\sim 100\,\mu\mathrm{s}$ (Fig. 3). As a result, the surrounding air and electrode materials (Cu and U) were heated, ionized or evaporated. The resultant gas/plasma largely consists of various components including molecules and ions of air, metal (Cu and U) ions and atoms, and perhaps also a small fraction of H, O, N and C released due to partial decomposition of the Kapton film. The materials deposited on glass plates in the arc discharge experiments to large extent depend on partial pressures (or densities) of the gas components, and on temperatures of the gas phase and the glass plates. Determination of those parameters is, therefore, the most important for revealing the mechanism controlling the deposition on the glass plates. To simplifying the analysis, we use the "effective metal" that has an atomic weight (84) weighted by the relative atomic fractions of Cu (0.88) and U (0.12) to replace the two metal components of Cu and U (Eq. (A1) in the Appendix), therefore, the gas/plasma is approximately treated as a binary-system of air and the effective metal. In the following context, "metal" used without specific definition refers to the "effective metal".

1. Shock wave and gas/plasma density

As the electric arc was triggered, the hot plasma ($T_g = 1.5\times10^4\,\mathrm{K}$) was generated immediately (on the time-scale of ns) between the electrode tips. In the same time the air right around the plasma was assumed to be heated to the same temperature as that of the plasma and accordingly a momentary high pressure (~50 atm) was established, driving

the gas/plasma to expand as a shock wave.[9] The shock wave propagates through air and glass plates in both horizontal and vertical directions (Fig. 2). Adopting a spherical wave approximation (Eq. (A3) in the Appendix), we estimate that propagation velocity of the shock wave front in air is $2.1\times10^{5}-1.5\times10^{6}\,\mathrm{cm/s}$ depending on the air temperature ahead of the shock front. The velocity in glass is $(3-4)\times10^{6}\,\mathrm{cm/s}$ without considering temperature elevation of the glass. These estimates are consistent with the experimental result of $1.6\times10^{5}-1.3\times10^{6}\,\mathrm{cm/s}$ in the previous study by time-resolved plasma imaging for the PMMA-Cu-air and the PETN-Cu-air plasma.[9]

The shock wave radially propagate out of the Kapton window space through the gaps between the glass plates and the Kapton film supporting the Cu-U electrodes (Fig. 2) until the pressure behind the shock front approaches the ambient pressure (~1 atm). Under the total pressure of $1\,\mathrm{atm}$ left in the gas space behind the shock front in between of the two glass plates (Fig. 2), we infer that at the temperature of $1.5\times10^{4}\,\mathrm{K}$, the total gas number density is $n_a + n_m = 5\times10^{17}\,\mathrm{cm^{-3}}$, where n_a and n_m are the number densities of the air molecules and the evaporated metal atoms, respectively. The relative amount of the metal atoms and the air molecules in the gas may vary during the arc discharge because of the deposition occurring on the glass plates. As an approximation, we assume that the partial pressure of the metal atoms in the gas is maintained by continuous evaporation of the electrodes during the $100\,\mu\mathrm{s}$ duration of the arc discharge. We also assume $n_a = n_m = 2.5\times10^{17}\,\mathrm{cm^{-3}}$. These densities are in agreement with that of $\sim10^{17}\,\mathrm{cm^{-3}}$ measured spectroscopically via Cu atomic emission for both the PMMA-Cu-air and the PETN-Cu-air plasma.[9]

2. *Temperature of glass plates and deposition during heating*

The glass plates depicted in Fig. 2 are initially at room temperature (300 K) and serve as a substrate for capturing the observed products (Figs. 7-10). During the arc discharge, the glass plates are heated by the combination effects of the thermal radiation, the molecular/atomic heat transfer and perhaps the latent heat due to metal condensation. We consider the plasma as a black body at the temperature of $T_g = 1.5 \times 10^4 \mathrm{K}$. According to the Stefan-Boltzmann law, therefore, the maximal thermal radiation flux generated is σT_g^4, where σ is the Stefan-Boltzmann constant. Absorption of the thermal radiation in a glass bulk is dependent on irradiation wavelength (λ) and determined by absorption coefficient of the glass, $\alpha(\lambda)$. Within the visible spectral region ($0.12\,\mu\mathrm{m} < \lambda < 8\,\mu\mathrm{m}$), absorption coefficient of pure silica glass is very small, $\alpha_{SiO2} = \sim 10^{-2}\,\mathrm{cm}^{-1}$, whereas it increases to $\sim 10^5\,\mathrm{cm}^{-1}$ at the UV edge ($\lambda \sim 0.12\mu\mathrm{m}$) and the far IR edge ($\lambda \sim 8\mu\mathrm{m}$) of this transparent band.[26] Excluding the contribution of the irradiation wavelengths within the transparent band, we integrate the Planck energy distribution function over wavelength and obtain the thermal radiation flux absorbed by the glass which is only $\sim 0.04\sigma T_g^4$, i.e. 4% of the maximal thermal radiation flux. This estimate indicates that the plasma radiation should not cause an appreciable heating in the pure silica glass. Deposition of metals (Cu and U) on the glass plates can, however, dramatically increase the radiation heating effect on the glass because absorption coefficient of Cu is continuously large: $\alpha_{\mathrm{Cu}} > 5.0 \times 10^5\,\mathrm{cm}^{-1}$ as $\lambda = 0.1 \sim 10\,\mu\mathrm{m}$[27] and that of U is expected to be similar. In other words, a very thin metal layer (< 0.5 μm thick) deposited on the glass plates can absorb nearly all the thermal radiation flux and causes heating of the glass.

At the glass/plasma interface, therefore, the net heat flux Q that causes heating of the glass can be approximately expressed as:

$$Q = \sigma[T_g^{\,4} - T(t)^4]\xi(t) + j_m\{\Delta H_m + 3k[T_g - T(t)]/2\} + j_a\, 3k[T_g - T(t)]/2\,. \qquad (1)$$

On the right-side of Eq. (1), the first term represents the heat flux originating from the hot plasma radiation, where $0 \le \xi(t) \le 1$ is an absorption factor due to the metal deposited on the glass plate. The absorption factor is a function of time in metal deposition process, and usually increases with deposition. The $T(t)$ is glass temperature at the time t after an electric arc is triggered, which initially is at room temperature, i.e., $T(t=0) = T_0 = 300\,\mathrm{K}$. The second term represents the heat flux due to heat transfer associated with the metal, including the latent heat of metal condensation (ΔH_m) and the kinetic energy exchange as a metal atom depositing on the glass plate ($3k[T_g - T(t)]/2$), where k is the Boltzmann constant. The j_m is the metal flux diffusing onto the surface of the glass plate from the hot gas/plasma. The third term represents the maximal molecular heat exchange rate due to the uncondensed air molecules together with a small addition of H_2, O_2 and N_2 from the decomposed Kapton film, in which we assume a complete exchange of kinetic energy occurs between the hot air molecules and the glass at the glass/plasma interface, i.e. the accommodation coefficient is equal to one. The j_a is the flux of the hot air molecules adjacent to the glass plate. Our quantitative estimations (Eqs. (A4)-(A10) in the Appendix) suggest that the heat fluxes calculated from the second and third terms in Eq. (1) are about one or two orders of magnitude lower than that from the first term, and that may elevate temperature of the glass to only ~450 K from 300 K. The expermental evidence (Figs. 7b & 8b), however, indicates that the glass was likely

liquefied during the arc discharge, implying that temperature of the glass should be much higher than 450 K since transition temperature of fused silica glass is 1,500 K[28] (for soda-lime glass, transition temperature varies with composition of the glass but is around ~1,000 K). Heating of the glass is, therefore, predominantly controlled by the thermal radiation absorbed by the deposited metal. We thus infer that a homogeneous metal film is likely formed on the cold glass plates by deposition at the very beginning of the arc discharge, probably occurring along with the propagation of the shock wave.

The deposited metal film plays the role of a surface heater on the glass plates. While it is being heated by absorbing thermal radiation from the hot plasma, the metal film is conducting the absorbed heat into the glass. As surface temperature of the glass plates rises, mobility of the deposited metal atoms on the glass surface increases and surface diffusion is activated. Since there is a large difference in surface energy between the metal and the silica glass (Cu: $1{,}200\,\mathrm{erg/cm^2}$ at 2,000 K;[29] U: $1{,}550\,\mathrm{erg/cm^2}$ at 1406 K;[30] and silica glass: ~ 230 to $270\ \mathrm{erg/cm^2}$ at 1,323 K.[31, 32]), the metal film is decomposed by the dewetting process[33] and forms islands and the spherical particles observed on the glass surface (Figs. 8c & 8d). Each of these particles grows in expending the metal atoms within a circular area having the radius of one surface diffusion path: $\sim 2\sqrt{D_s t}$, where D_s is the effective surface diffusivity of the metal on glass. When the diameter of a spherical particle, $2R$, exceeds the metal absorption length, $1/\alpha_m$, the particle absorbs all the radiation impinging on its cross-section πR^2, whereas the rest of the glass surface is nearly free of the metal and approximately transparent for the

radiation. Under this situation, the absortion factor, $\xi(t)$, is determined as the coverage fraction of metal particles over the glass surface:

$$\xi(t) = \pi R^2 / L^2 = (3\sqrt{\pi}\, j_m \omega_m / 16\sqrt{D_s})^{2/3} t^{1/3}. \quad (2)$$

In Eq. (2), $L = 4\sqrt{D_s t}$ is the average distance between two adjacent particles (center to center) and L^2 is the area of glass surface per particle. The mass conservation law: $4\pi R^3 / 3 = L^2 \bar{h}$ is applied, where $\bar{h} = j_m \omega_m t$ is the average thickness of the metal film deposited on the glass surface at the time *t*, and $\omega_m = 1.4 \times 10^{-23}\text{cm}^3$ is the atomic volume of the metal.

In order to estimate the temperature of glass at surface of the glass plates, we assume that at the time t the absorbed radiation flux, $\xi(t)\sigma T_g^{\,4}$, is spread into the glass only within one thermal diffusion length ($2\sqrt{at}$) depth from the surface of the glass plates, where a is the thermal diffucivity of glass. We, therefore, have

$$dT(t)/dt = Q / 2c_p \rho \sqrt{at} = \sigma T_g^{\,4} \xi(t) / 2c_p \rho \sqrt{at}, \quad (3)$$

where c_p and ρ are mass heat capacity and density of the glass, respectively. In Eq. (3), we neglect the heat contributions from the second and the third terms in Eq. (1), and also ignore the $T(t)$ in the first term because of $T(t) << T_g$. Substituting Eq. (2) into Eq. (3) and solving the differential equation, we have

$$T(t) = T_0 + (6/5)(t/\tau)^{5/6} T_g, \quad (4a)$$

$$\tau \equiv (2c_p \rho \sqrt{a} / \sigma T_g^{\,3})^{6/5} (16\sqrt{D_s} / 3\sqrt{\pi} j_m \omega_m)^{4/5}. \quad (4b)$$

Taking the effective surface diffusivity to be: $D_s = 10^{-6}\,\mathrm{cm}^2/\mathrm{s}$, we obtain that the glass temperature of the surface layer is $\sim 2.3\times10^{3}\,\mathrm{K}$ by the end of the arc duration time of $t = 10^{-4}\,\mathrm{s}\,(100\ \mu\mathrm{s})$. Correspondingly, the absorption factor is $\xi(100\,\mu\mathrm{s}) = 0.18$, falling in the range of 0.02-0.2 that is experimentally determined from the SEM images (Figs. 7 & 8). The estimated results suggest that the glass at the plate surface may be liquefied during the arc discharge, which is consistent with our experimental observations (Figs. 7b & 8b).

While the surface diffusion of the metal atoms occurs on surface of the glass plate, the metal atoms can also diffuse into the glass bulk, especially under the liquefied state. According to Eqs. (4a) and (4b), it is found that the glass of a surface layer liquefies in $\sim 3.0\times10^{-5}\,\mathrm{s}\,(30\ \mu\mathrm{s})$ after onset of the arc discharge as we assume transition temperature of the glass is $1{,}000\,\mathrm{K}$. Metal diffusivity in liquefied glass (D_ℓ) typically is in the range of $10^{-6} - 10^{-4}\,\mathrm{cm}^2/\mathrm{s}$. Thus, during the rest of arc duration time, $\tau = \sim 7.0\times10^{-5}\,\mathrm{s}\,(70\ \mu\mathrm{s})$, metal atoms may penetrate the glass to the depth of $2\sqrt{D_\ell\tau} = \sim 0.2 - 2.0\,\mu\mathrm{m}$. The depth is in agreement with the observation shown in Figs. 10a and 10c, in which the UO_2 particles likely form by reaction between U atoms and the surrounding oxygen because of the strongest affinity (the Pauling's electronegativity is 3.5 for O, 1.8 for Si, 1.9 for Cu and 1.4 for U).

To summarize, a thin metal film forms on the initially cold glass plates by deposition at the very beginning of onset of the electric arc, and then is decomposed to form islands due to the dewetting as surface temperature of the glass plates increases. The metal atomes deposited on the glass plates diffuse both on the surface and into the

liquefied glass layer at the surface of the glass plates. These diffusions are accompanied by chemical reactions that result in the recovered materials at the glass plates (Figs. 7-10). Here, we also want to point out that the products may slightly alters during the cooling (after the arc duration), and we are unable to complately exclude that a small population of the products may be formed by condensation.

E. Materials recovered from the Kapton film

As previously discussed, the morphology of the window in the Kapton backing is largely unaffected by the arc (c.f. Figs. 4a, and 5a). Figures 11a and 11b are low magnification backscattered electron SEM images taken from the Kapton film near an electrode tip after the arc discharge. These images indicate that the Kapton film has sustained damage due to ablation. Abundant uranium-containing materials were recovered on the Kapton film, some of which appear to be embedded, as indicated by arrows on Figs. 11a and 11b. Much of the material recovered from the Kapton film takes the form of spherules (Figs. 11c, 11d, and 11f-h). Three of these spherules, S-1 (Fig. 11f), S-2 (Fig. 11g) and S-3 (Fig. 11h) were selected for additional TEM analysis.

Figure 12 shows the results of TEM observations: Figs. 12a, b and c are bright-field TEM images of cross sections of spherules S-1, S-2 and S-3, respectively; Figs. 12d, e and f are the corresponding EDS elemental maps of U-$L_{\alpha 1}$; Figs. 12g and h are EDS elemental maps of Cu-$K_{\alpha 1}$ for the spherules S-1 and S-2; and Fig. 12i is an elemental map of O-$K_{\alpha 1}$ for spherule S-3. These images show that each spherule has a uranium-rich rim or shell with varying thickness for the different spherules. Spherules S-1 (Fig. 12a) and S-2 (Fig. 12b) also contain uranium-rich inclusions embedded in a copper matrix. Spherule

S-3, however, has a hollow structure (Fig. 12c). Electron diffraction analysis indicates that the uranium-rich rims are crystalline, and form a single crystal for each spherule. Figures 12j-l are selected-area electron diffraction patterns taken from the uranium-rich rim of the spherule S-2. All the patterns can be indexed as *fcc* UO_2.

Uranium-rich inclusions are homogeneously distributed in spherules S-1 (Fig. 12a) and S-2 (Fig. 12b). Enlarged bright-field TEM images (Figs. 13a and 13b) show that these uranium-rich inclusions display a dark contrast and have a cuboidal shape and size of 50-100 nm. EDS elemental mapping indicates the uranium-rich inclusions are embedded in a polycrystalline copper matrix (Figs. 13b-f). The copper matrix of the spherule S-1 consists of large equal-axis copper grains (Fig. 12a), while the copper grains of spherule S-2 display elongated shapes (Figs. 12b and 13b). In addition, segregation of a uranium-rich phase can be identified at the grain boundaries of copper in spherule S-2 (Figs. 13e-f).

To determine the crystal structure of the uranium-rich inclusions, electron microdiffraction was employed. A series of electron microdiffraction patterns collected from different individual inclusions (Figs. 14a and 14b) are shown in Figs. 14c-h. All the patterns can be indexed to match the crystal structure of α-UC_2 (tetragonal, *I4/mmm* (139), a = 3.509(3) Å and c = 5.98(5) Å).[34] One of the diffraction patterns, shown in Fig. 14c, also matches the crystal structure of UC (cubic, $Fm\bar{3}m$ (225), a = 4.951±0.001 Å)[35], as well as that of UO (cubic, $Fm\bar{3}m$ (225), a = 4.92±0.02 Å).[35] EDS analysis of the uranium-rich inclusions indicates dominant uranium and copper peaks, with no significant oxygen. The carbon K_α peak (277 eV)[36] overlaps one of the *N* series uranium peaks ($N_{VI}O_{IV}$: 286 eV)[36] at the ~130 eV energy resolution of the EDS system. We

conclude that the uranium-rich inclusions are α-UC_2, although we are unable to exclude the possibility of the coexistence of UC. The α-UC_2 is believed to form from a reaction of uranium with the carbon originating from the Kapton ($C_{22}H_{10}N_2O_5$) film, but how UC_2 mixes with copper under these conditions remains an open question, as does the formation of the UO_2 coating on the spherules. Further investigation is needed to address these questions.

IV. CONCLUSION

We used an electric arc to generate a uranium-containing plasma in air. The recovered solid debris was analyzed using electron beam-based diagnostics in combination with a theoretical estimation. The device for generating the arc is compact, requires only very small samples and allows arc durations of up to ~ 100 μs, while achieving temperatures near or above 1 eV. The recovered material was strongly affected by the environment with which the heated material interacted. Different combinations of the primary elements (Cu, U, Si, O, C) were observed, depending on the recovery location, while the debris predominantly exhibited the morphology of spherules having a wide range of sizes, compositions and structures. Theoretical analysis suggests that a high temperature is developed immediately after onset of the plasma and creates a momentary high pressure, leading to the plasma expanding as a shock wave through the narrow gaps between the glass plates and the Kapton-Cu-U sheet. During the passage of the shock wave propagation, a thin metal film likely forms on the initially cold glass plates by deposition, and then is decomposed to form metal islands due to the dewetting as the temperature increases. The glass plates are heated mainly by thermal radiation of the

plasma absorbed by the metal islands deposited on the glass plates. The surface temperature of the glass plates may rise to $\sim 2{,}300\,\mathrm{K}$ during the arc discharge, resulting in liquefying of a glass layer of the surface. The metals deposited on the hot glass plates may diffuse both on the surface and into the liquefied glass layer. These diffusions are accompanied by chemical reactions that result in the recovered materials at the glass plates (Figs. 7-10).

This experimental system provides a reasonable approximation of a scaled temperature field simulating the conditions relevant to fallout formation in a cooling cloud produced by a near-surface nuclear detonation. The recovered materials were characterized with respect to morphology, composition, spatial relationships, crystallinity and structure to provide insight into the physical and chemical formation environment relevant to fallout. This work, therefore, provides a new approach to understanding the formation of fallout following an event in which uranium or other actinide containing materials interact with the environment at high temperature, followed by rapid cooling.

A number of improvements could be made to the current approach to improve its applicability. Sample fabrication utilized well-established thin-film deposition technology. Future sample-electrode multilayer films could be made containing combinations of elements more relevant to nuclear devices (e.g. U, Fe and W, with much less or no Cu). Here, we used glass as the primary recovery substrate. Other insulating materials could also be used, as long as the plasma remained optically accessible for temperature measurement. Also, changing the position of the substrate with respect to the arc may allow different cooling rates to be investigated. In this work we only measured the temperature in one location of the arc and did not investigate the relationship between the

location-dependent nature of the recovered material to spatially resolved temperature and cooling rate. It should be possible to map the arc in time and temperature, thus establishing a relationship between point of recovery and time – temperature history. Finally, the arc duration, although substantially lengthened for this work, does not yet match the cooling times scales of tenths to tens of seconds over which eV temperatures cool to the point at which silicate materials solidify, applicable to fallout formation. Small modifications to the existing system could increase the lifetime of the arc to ~0.5 ms, however, and thus at least provide a wide range of scalable times over which actinide behavior under high temperature, rapidly cooled regimes could be evaluated.

ACKNOWLEDGEMENTS

We acknowledge P. G. Allen for useful discussion and advice. We are grateful to R. Forman for advice concerning the deposition of the uranium film. We thank J. M. Zaug and Nick E. Teslich for assistance with the arc experiments and preparation of TEM samples, respectively. We also thank Joel Stanley for upgrading the pulser for long-pulse operation. This work was performed under the auspices of the U. S. Department of Energy by Lawrence Livermore National Security, LLC under Contract DE-AC52-07NA27344 and supported by the Laboratory Directed Research and Development Program (10-SI-016) at LLNL.

APPENDIX

1. Atomic weight and mass of effective metal

As discussed in the Section III-B, the U-coated Cu-electrodes (Fig. 2) have the average composition by mass of $\mathrm{Cu} : \mathrm{U} = 2 : 1$, resulting in the relative atomic fractions

0.88 and 0.12 for Cu and U, respectively. Atomic weight of the effective metal is weighted by the relative atomic fractions of Cu and U, thus, is

$$0.88 \times 63 + 0.12 \times 238 = 84, \tag{A1}$$

where Cu and U atomic weights are 63 and 238, respectively. Atomic mass of the effective metal is

$$m_m = 84 \times 1.67 \times 10^{-24}\ \mathrm{g}. \tag{A2}$$

2. ***Propagation velocity of shock wave***

Under the approximation of a spherical wave, propagation velocity of the shock wave can be expressed by[37]

$$U = c_o[1 + (\gamma + 1)P / 2\gamma P_0]^{1/2}, \tag{A3}$$

where, c_o is speed of sound in the medium ahead of the shock wave front, γ is the ratio of the specific heats of the medium, P is the overpressure behind the shock wave front, and P_0 is the ambient pressure (1 atm). The speed of sound in air is determined by $c_o = (\gamma kT / m_a)^{1/2}$, where T is the air temperature immediately ahead of the shock front; $\gamma = 1.4$ at room temperature and $1 < \gamma < 1.09$ above ~2,500K; k is the Boltzmann constant; and m_a is the average mass of air molecule ($m_a = 29 \times 1.67 \times 10^{-24}\ \mathrm{g}$). At $P / P_0 = 50$ and $300 < T < 1.5 \times 10^4\ \mathrm{K}$, Eq. (A3) gives: $2.1 \times 10^5 < U < 1.5 \times 10^6\ \mathrm{cm/s}$. Here we ignore the additional pressure increase due to evaporated Cu and U because of the very fast onset of the plasma. For the case of glass, $c_o = (3.96 - 5.64) \times 10^5\ \mathrm{cm/s}$ depending on composition of the glass, and $\gamma = 1.0$, we thus estimate that the shock velocity is $\sim (3 - 4) \times 10^6\ \mathrm{cm/s}$ without considering temperature elevation of the glass.

3. *Thermal diffusivity of glass*

Fused silica (SiO_2) glass at room temperature has the density: $\rho = 2.2\,\mathrm{g/cm^3}$, the mass heat capacity: $c_p = 0.17\mathrm{cal/g\,K}$, and the thermal conductivity: $\kappa = 3.3\times10^{-3}\mathrm{cal/cm\,s\,K}$. The thermal diffusivity of the glass is given by

$$a = \kappa / \rho c_p = 8.9\times10^{-3}\mathrm{cm^2/s}. \quad \text{(A4)}$$

4. *Fluxes of metal atom and air molecule in gas/plasma*

The impinging fluxes, j_a and j_m, are controlled by molecular/atomic diffusion of the binary-system of air and metal. Adopting the Chapman-Enskog formula to calculate the gas diffusivity, *D*, we obtain

$$j_{a,m} = Dn_{a,m}/H = [3n_{a,m}/2H(n_a+n_m)(d_a+d_m)^2][kT_g(m_a+m_m)/2\pi m_a m_m]^{1/2}. \quad \text{(A5)}$$

Here, $n_{a.m}$ represent density of air (n_a) or density of metal (n_m) in the bulk gas/plasma. H ($\approx 100\mu m$) is the effective distance between the two glass plates, and $d_{a,m}$ and $m_{a,m}$ are, respectively, the collision diameters and masses of the air molecule (d_a and m_a) and the metal atom (d_m and m_m) in the gas/plasma. Under these assumptions, Eq. (A5) yields $j_a = j_m = 1.7\times10^{21}\,1/\mathrm{cm^2 s}$.

5. *Maximal thermal radiation flux*

For a black body at the temperature of $T_g = 1.5\times10^4\mathrm{K}$, according to the Stefan-Boltzmann law, the maximal thermal radiation flux is

$$\sigma T_g^{\,4} = 6.9\times10^4\,\mathrm{cal/cm^2 s}. \quad \text{(A6)}$$

$\sigma = 1.36\times10^{-12}\,\mathrm{cal/cm^2 s K^4}$ is the Stefan-Boltzmann constant.

6. Latent heat and energy exchange between gas molecule/atom and glass

The latent heat of the effective metal condensition is estimated to be $\Delta H_m = 85\,\text{kcal/mol}$ from the latent heats of Cu: $\Delta H_{Cu} = 81\,\text{kcal/mol}$ and U: $\Delta H_U = 116\,\text{kcal/mol}$, weighted by the relative atomic fractions of Cu and U in the original electrodes. The heat flux associated with the metal is calculated as

$$j_m(\Delta H_m + 3kT_g/2) = 3.7\times10^2\ \text{cal/cm}^2\text{s}. \tag{A7}$$

Correspondingly, we can deduce from Eq. (3) that this heat flux may cause a temperature increase on the glass of

$$T - T_0 = [j_m(\Delta H_m + 3kT_g/2)/\sqrt{2}c_p\rho]\,t^{1/2} = 105\,\text{K}. \tag{A8}$$

The maximal molecular heat exchange between air molecules and the glass is

$$j_a(3kT_g/2) = 1.3\times10^2\ \text{cal/cm}^2\text{s}. \tag{A9}$$

The corresponding temperature increase on the glass is then

$$T - T_0 = [j_a(3kT_g/2)/\sqrt{2}c_p\rho]\,t^{1/2} = 36\,\text{K}. \tag{A10}$$

REFERENCES

1. N. Eby, R. Hermes, N. Charnley and J. A. Smoliga, Geology Today **26** (5), 180-185 (2010).
2. A. J. Fahey, C. J. Zeissler, D. E. Newbury, J. Davis and R. M. Lindstrom, P Natl Acad Sci USA **107** (47), 20207-20212 (2010).
3. S. Glasstone and P. J. Dolan, in *The Effects of Nuclear Weapons* (The United States Department of Defense and The United States Department of Energy, 1977), pp. 387-450.
4. C. E. Adams, N. H. Farlow and W. R. Schell, Geochim Cosmochim Ac **18** (1-2), 42-56 (1960).
5. I. J. Russell, in *Operation Sun Beam Shot Johnie Boy Project Officers Report - Project 2.13* (Operation Sun Beam Shot Johnie Boy Project Officers Report - Project 2.13, 1965), pp. 125-xxx.
6. R. E. Heft, Adv Chem Ser (93), 254-281 (1970).

7. K. Stewart, T Faraday Soc **52** (2), 161-173 (1956).
8. P. B. Storebo and C. Rho, J Geophys Res **75** (15), 2931-2938 (1970).
9. V. Tang, C. D. Grant, J. F. McCarrick, J. M. Zaug, E. A. Glascoe and H. Wang, J Appl Phys **111**, 053303 (2012).
10. G. Spriggs, Report No. LLNL-PRES-468671, February, 2011.
11. The electrodes are made by Altaflex company, http://www.altaflex.com/.
12. A. F. Goncharov and J. C. Crowhurst, Rev Sci Instrum **76** (6), 063905 (2005).
13. L. A. Giannuzzi and F. A. Stevie, *Introduction to Focused Ion Beams, Instrumentation, Theory, Techniques and Practice*. (Springer, 2004).
14. J. J. Katz and E. Rabinowitch, *The Chemistry of Uranium Part I The Element, Its Binary and Related Compounds*, 1st ed. (McGraw-Hill Book Company, Inc., New York - Toronto - London, 1951).
15. I. Grenthe, J. Drozdzynski, T. Fujino, E. C. Buck, T. E. Albrecht-Schmitt and S. F. Wolf, in *The Chemistry of the Actinide and Transactinide Elements*, edited by L. R. Morss, N. M. Edelstein and J. Fuger (Springer, Dordrecht, 2010), Vol. 1, pp. 253-698.
16. C. W. Jacob and B. E. Warren, J Am Chem Soc **59**, 2588-2591 (1937).
17. R. W. G. Wyckoff, *Crystal Structures*, 2nd ed. (John Wiley & Sons, New York - Toronto - Sydney, 1963).
18. N. C. Baenziger, R. E. Rundle, A. I. Snow and A. S. Wilson, Acta Crystallogr **3** (1), 34-40 (1950).
19. H. A. Wilhelm and O. N. Carlson, T Am Soc Metal **42**, 1311-1325 (1950).
20. F. A. Rough and A. A. Bauer, Report No. BMI-1300 / UC-25 Metallurgy and Ceramics, 1958.
21. R. W. Olesinski and G. A. Abbaschian, in *Binary Alloy Phase Diagrams*, edited by T. B. Massalski (Editor-in-Chief), H. Okamoto, W. W. WScott, M. A. Fleming and R. Boring (ASM International / The Materials Information Society, 1990), Vol. 2, pp. 1477-1478.
22. M. Kurihara, M. Hirata, R. Sekine, J. Onoe and H. Nakamatsu, J Nucl Mater **326**, 75-79 (2004).
23. H. E. Swanson and E. Tatge, Nat Bur Stand (U.S.) **2**, 33-35 (1953).
24. K. P. Mukherjee and J. Bandyopadhyaya, Transactions of the Metal Society, the American Institute of Mining and Metallurgical Engineers **245**, 2335-2338 (1969).
25. N. Mattern, R. Seyrich, L. Wilde, C. Baehtz, M. Knapp and J. Acker, J Alloy Compd **429** (1-2), 211-215 (2007).
26. R. Kitamura, L. Pilon and M. Jonasz, Appl Optics **46** (33), 8118-8133 (2007).
27. E. D. Palik, in *Handbook of Optical-Constants of Solids* (Academic Press, Orlando, 1985), pp. 280-286.
28. J. A. Bucaro and H. D. Dardy, J Appl Phys **45** (12), 5324-5329 (1974).
29. D. A. Harrison, D. Yan and S. Blairs, J Chem Thermodyn **9** (12), 1111-1119 (1977).
30. J. A. Cahill and Kirshenb.Ad, J Inorg Nucl Chem **27** (1), 73-76 (1965).
31. S. K. Rhee, J Mater Sci **12** (4), 823-824 (1977).
32. C. W. Parmelee, L. C. Lyon and C. G. Haman, U. of Illinois Bulletin **XXXVI** (N81), 1-58 (1939).
33. D. Bonn, J. Eggers, J. Indekeu, J. Meunier and E. Rolley, Rev Mod Phys **81** (2), 739-805 (2009).
34. A. E. Austin, Acta Crystallogr **12** (2), 159-161 (1959).
35. R. E. Rundle, N. C. Baenziger, A. S. Wilson and R. A. Mcdonald, J Am Chem Soc **70** (1), 99-105 (1948).
36. J. A. Bearden, Rev Mod Phys **39** (1), 78-124 (1967).
37. S. Glasstone and P. J. Dolan, in *The Effects of Nuclear Weapons* (The United States Department of Defense and The United States Department of Energy, 1977), pp. 97-98.

Figures and captions

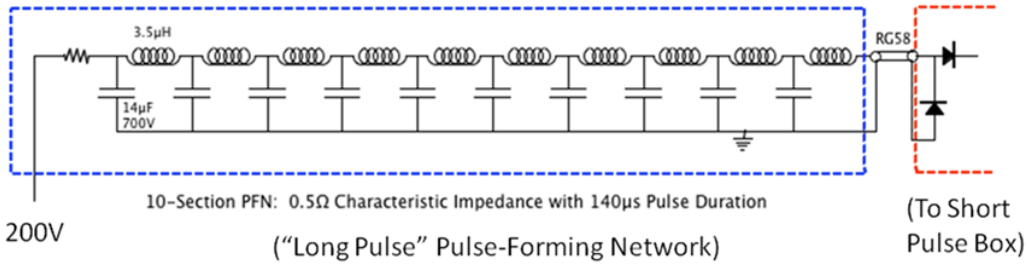

FIG. 1. A schematic of the pulse-forming network used to generate the comparatively long-lived (~100 μs) plasmas of this work. This component represents an extension to the previous design of Tang et al. which generated a shorter-lived plasma.[9]

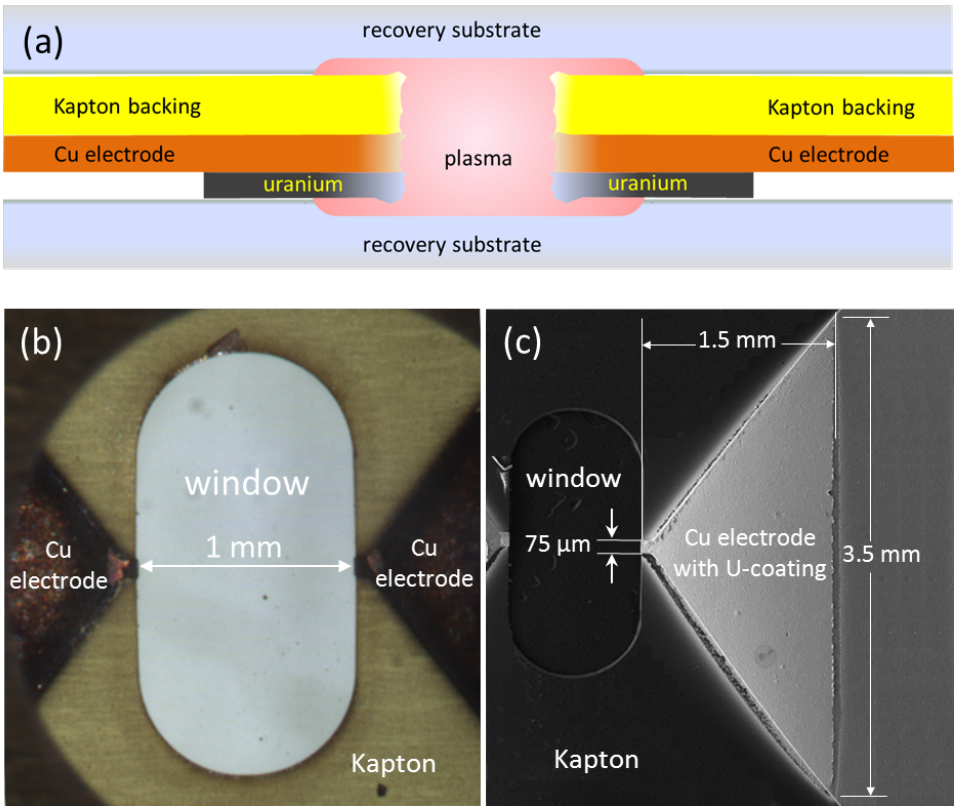

FIG. 2. Configuration of the spark gap and uranium thin film samples. (a) A side view schematic diagram showing the relative positions of the copper electrodes, uranium film, Kapton backing, and recovery substrates. (b) Plan view optical image of an electrode pair forming a point-to-point breakdown gap of 1 mm. The light yellow film is the ~25 µm-thick Kapton backing. The clear region between the tips is an open window on the Kapton film. (c) SEM image of an electrode tip showing the in-plane dimensions of the deposited uranium film. The thickness of the U film was ~ 4 µm.

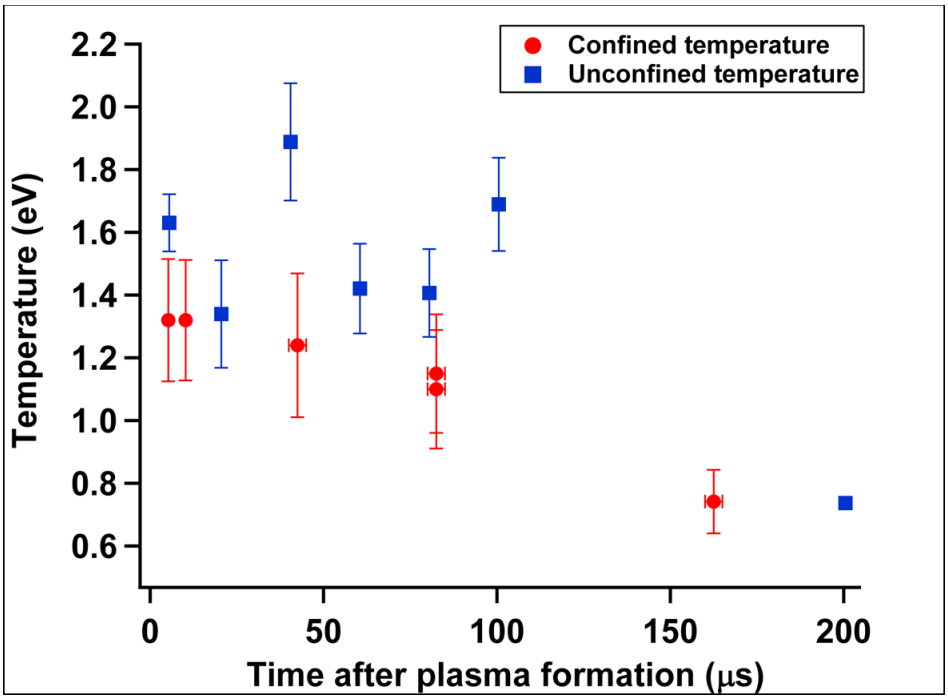

FIG. 3. Time-resolved temperature data as derived from Cu(I) atomic emission lines and corresponding gate widths (*x*-axis "error" bars) as a function of time after plasma formation (μs). The red-dot data points are for the case of plasma confined between glass plates, of which gate widths are 0.5 μs for the 5 and 10 μs delay points (too short to show up on the *x*-scale of the figure) and 5 μs for every data point thereafter. The blue-square data points are for the case of unconfined plasma, of which gate widths are 1μs for every data point (too short to show up on the *x*-scale of the figure). The reason that there is apparently no *y*-error bar for the last blue data point is because, like the gate width, the value is too small to show up on the *y*-scale of the figure.

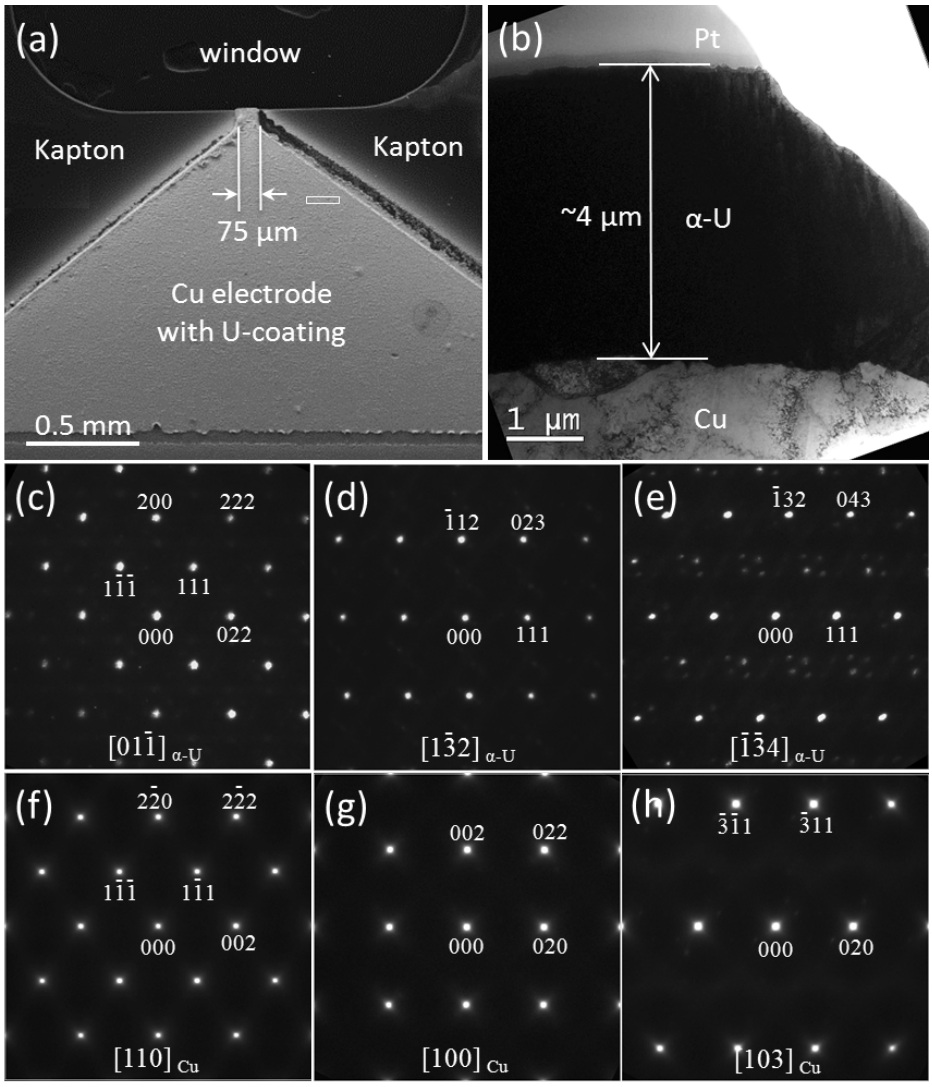

FIG. 4. (a) Backscattered electron SEM image of an electrode tip before an arc. The white rectangle in Fig. 4a indicates the region from which a section for TEM analysis was extracted by FIB. (b) Bright-field TEM image of the cross section from Fig. 4a. The Pt coating was introduced during TEM sample preparation by FIB to protect the sample from ion-beam damage. (c)-(e) Selected area electron diffraction patterns taken from the uranium film, which can be indexed as $[01\bar{1}]$, $[1\bar{3}2]$ and $[\bar{1}\bar{3}4]$ zones of α-uranium metal. (f)-(h) Selected-area electron diffraction patterns taken from copper and indexed as [110], [100] and [103] zones of *fcc* copper crystal.

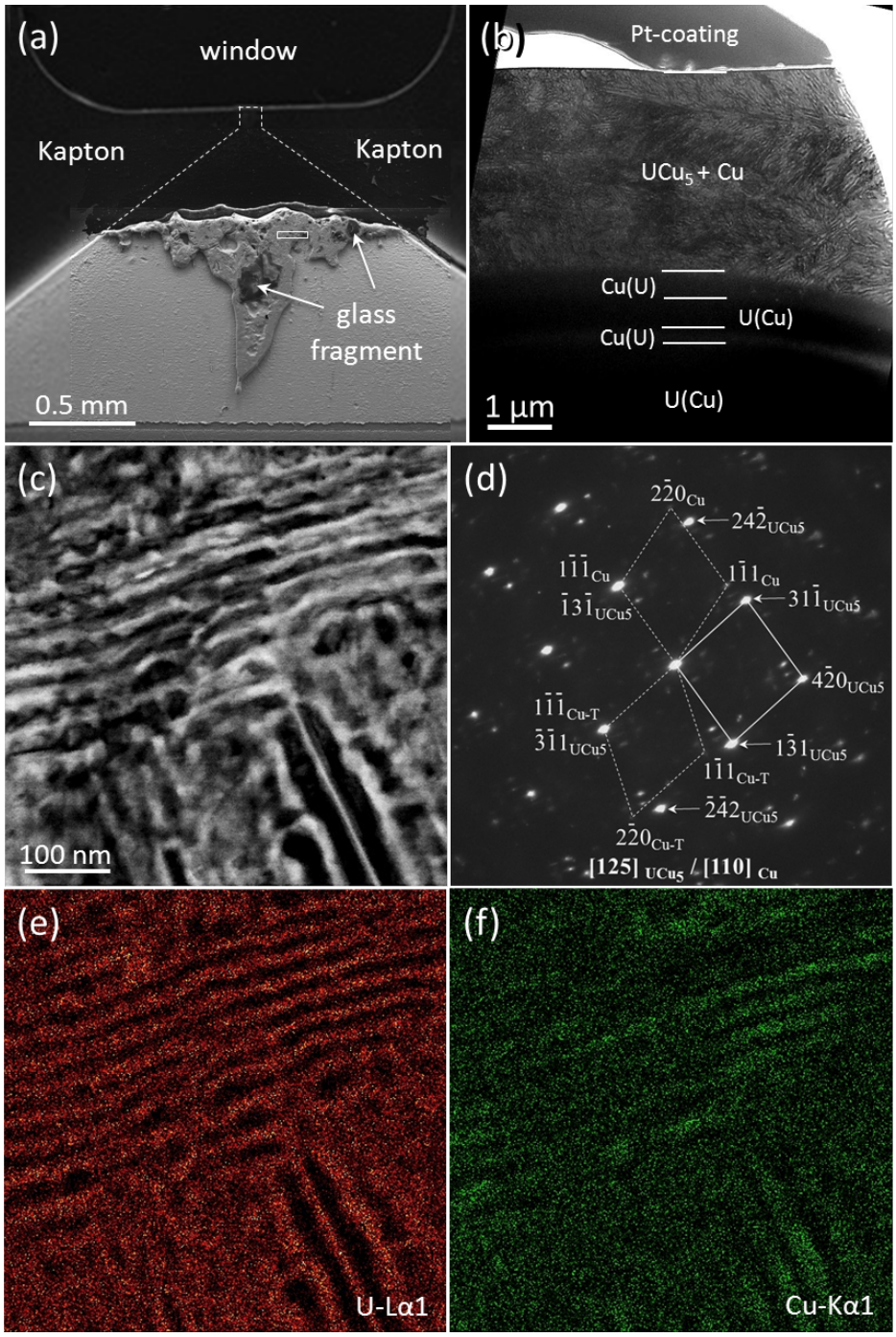

FIG. 5. (a) Backscattered electron SEM image of an electrode tip after an arc. The white rectangle in Fig. 5a indicates the region from which sample for TEM analysis was extracted using the FIB. (b) Bright-field TEM image of the cross section extracted from the white box in Fig. 5a. The Cu(U) and U(Cu) denote Cu-rich and U-rich phases, respectively. (c) Z-contrast dark-field STEM image of an area within the top layer (UCu_5 + Cu). (d) Selected-area electron diffraction pattern

taken from the top layer (UCu_5 + Cu) in image (b). The parallelogram of solid lines is a repeated unit of the [125] zone of UCu_5. The parallelograms of dashed lines are repeated units of the [110] zones of copper. The subscript Cu-T refers to a copper twin. (e) & (f) X-ray EDS elemental maps of U-Lα1 and Cu-Kα1, which correspond to the same area of (c).

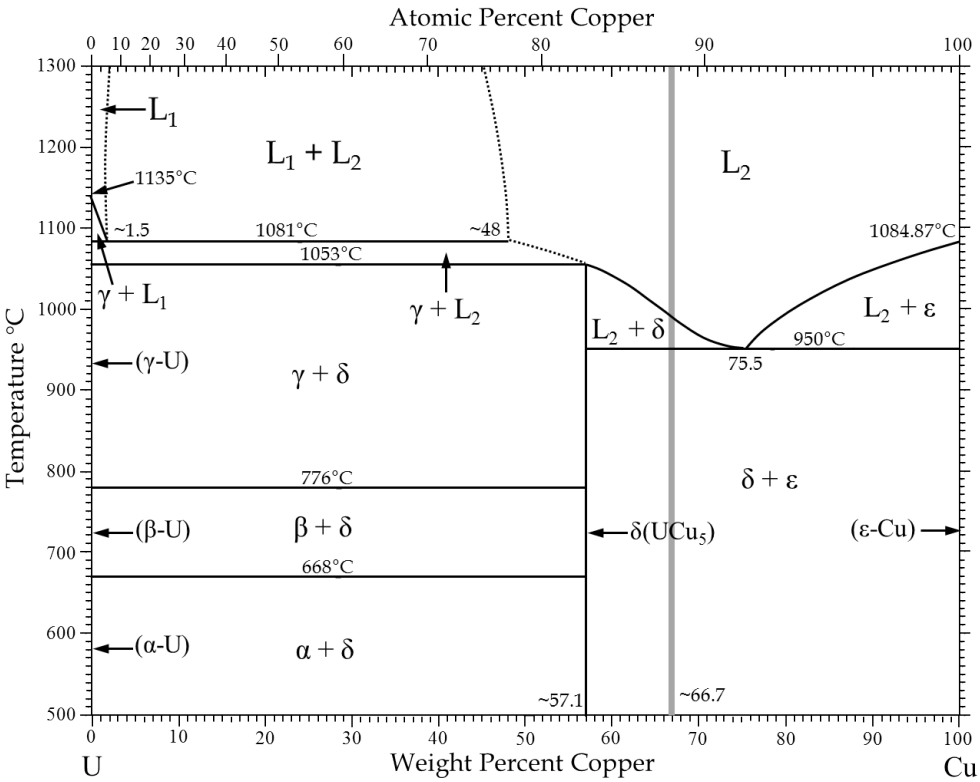

FIG. 6. Copper-uranium equilibrium phase diagram modified from the version shown in ASM binary alloy phase diagrams.[21] The gray line located at ~66.7% indicates average composition of the ablated electrode tip.

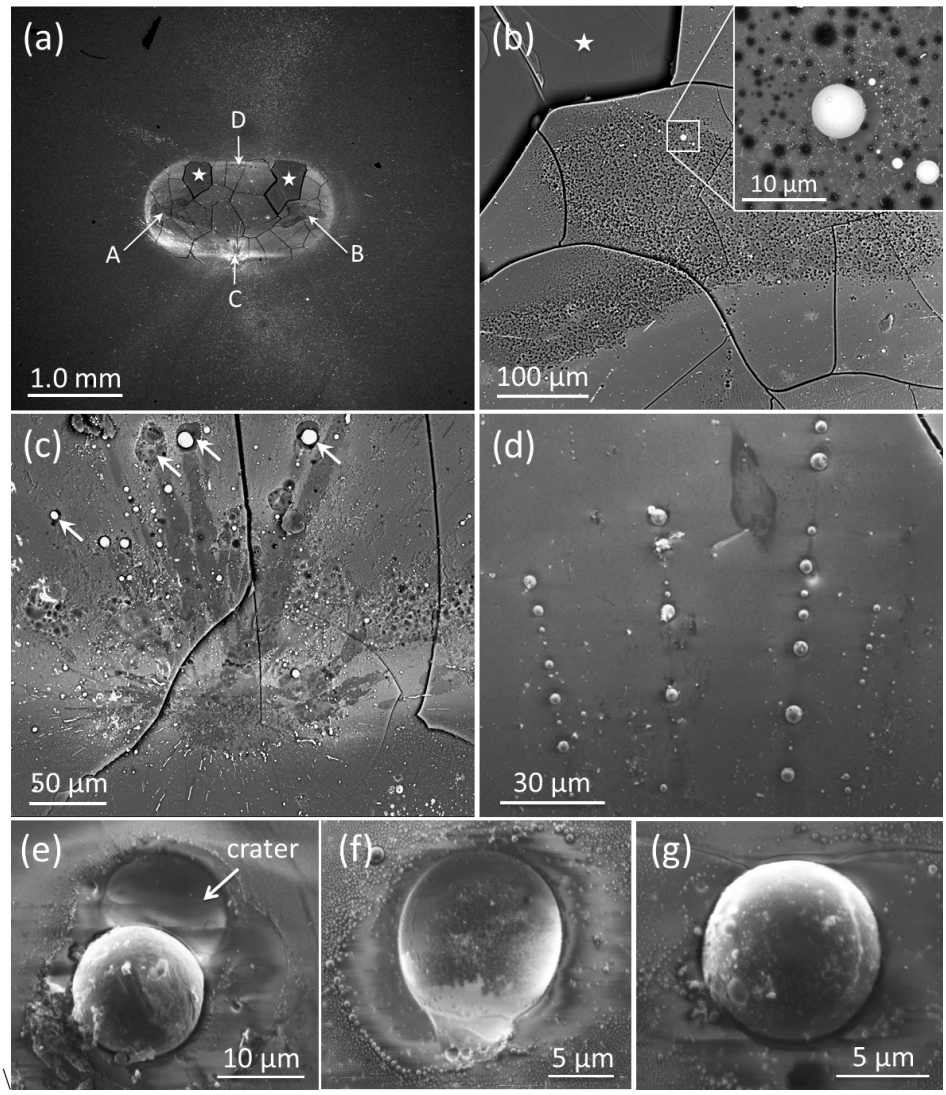

FIG. 7. (a) Low magnification backscattered electron SEM image of the top glass plate. Glass fragments were peeled off at the darker areas indicated by asterisks. (b) and (c) Backscattered electron SEM images showing morphologies of the areas around the arrowheads B and C of (a), respectively. Image (c) shows U-rich spherules that appear to have been created by a larger primary impactor. The morphology of the craters suggests the glass was softened or partially molten at the time of impact. The inset in (b) is an enlarged image corresponding to the area of the white-line box. (d) Secondary electron SEM image from the region above C of (a). (e)-(g) High magnification secondary electron SEM images showing typical morphology of spherules found on the top glass plate.

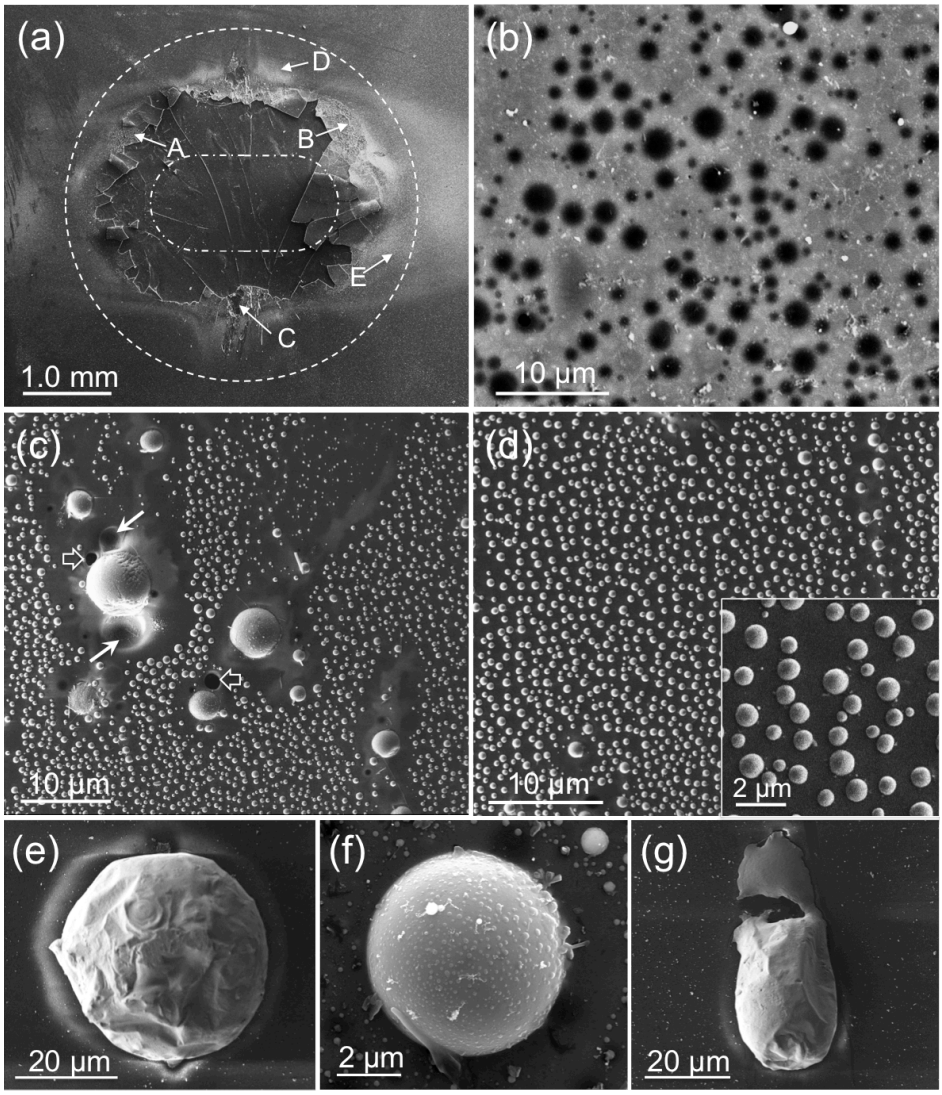

FIG. 8. (a) Low magnification secondary electron SEM image of the bottom glass plate. The figure drawn with the dotted and dashed line indicates the position of the window on the Kapton film (see Fig. 2b). The outer dashed circle has a radius of ~2 mm. (b) Backscattered electron SEM image showing morphology of the area around the arrowhead B of (a). (c)-(d) Secondary electron SEM images taken from the regions of D and E of (a), respectively. Inset of (d) is an enlarged image. (e)-(g) High magnification secondary electron SEM images showing typical morphology of spherules found on the bottom glass plate.

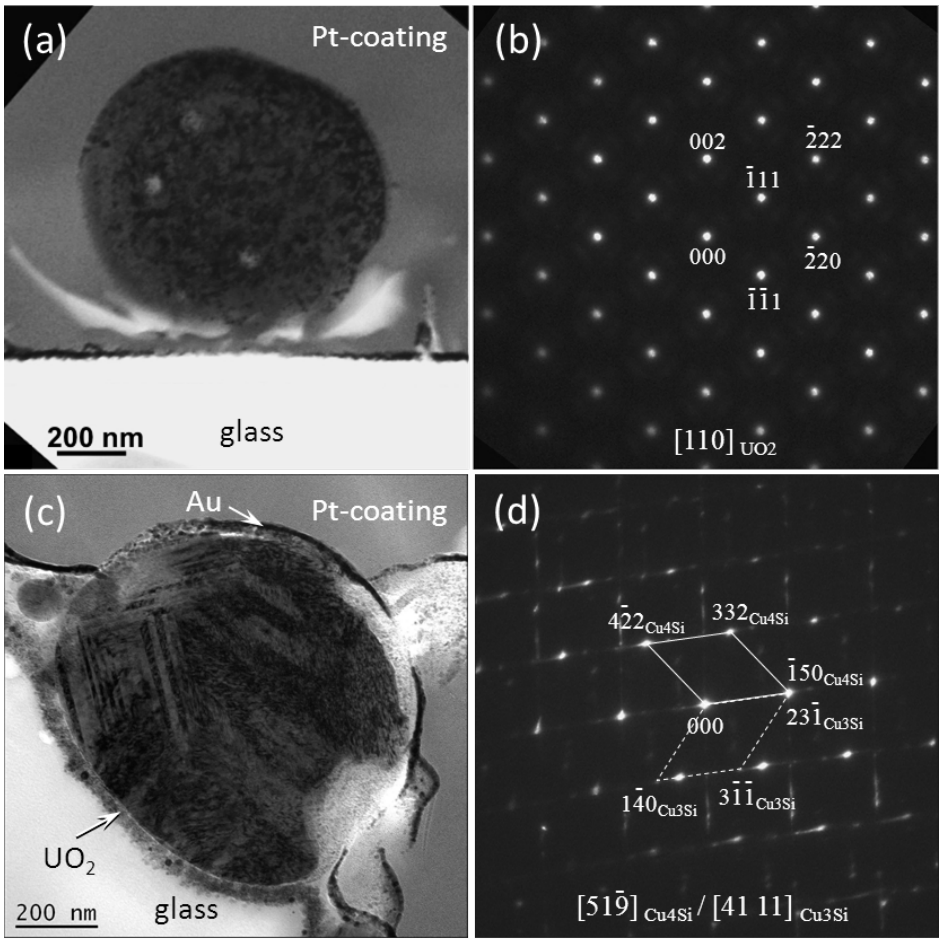

FIG. 9. (a) Bright-field TEM image of a spherule resting on the bottom glass plate. (b) A corresponding selected-area electron diffraction pattern that can be indexed as the [110] zone of UO_2. (c) Bright-field TEM image of a spherule partially embedded in the bottom glass plate. The Au layer was deposited to reduce charging effects and thus improve the SEM image. (d) A corresponding selected-area electron diffraction pattern. The parallelogram of solid lines is a repeated unit of the $[51\bar{9}]$ zone of ε-Cu_4Si. The parallelogram of dashed lines is a repeated unit of [41 11] zone of η′′-Cu_3Si.

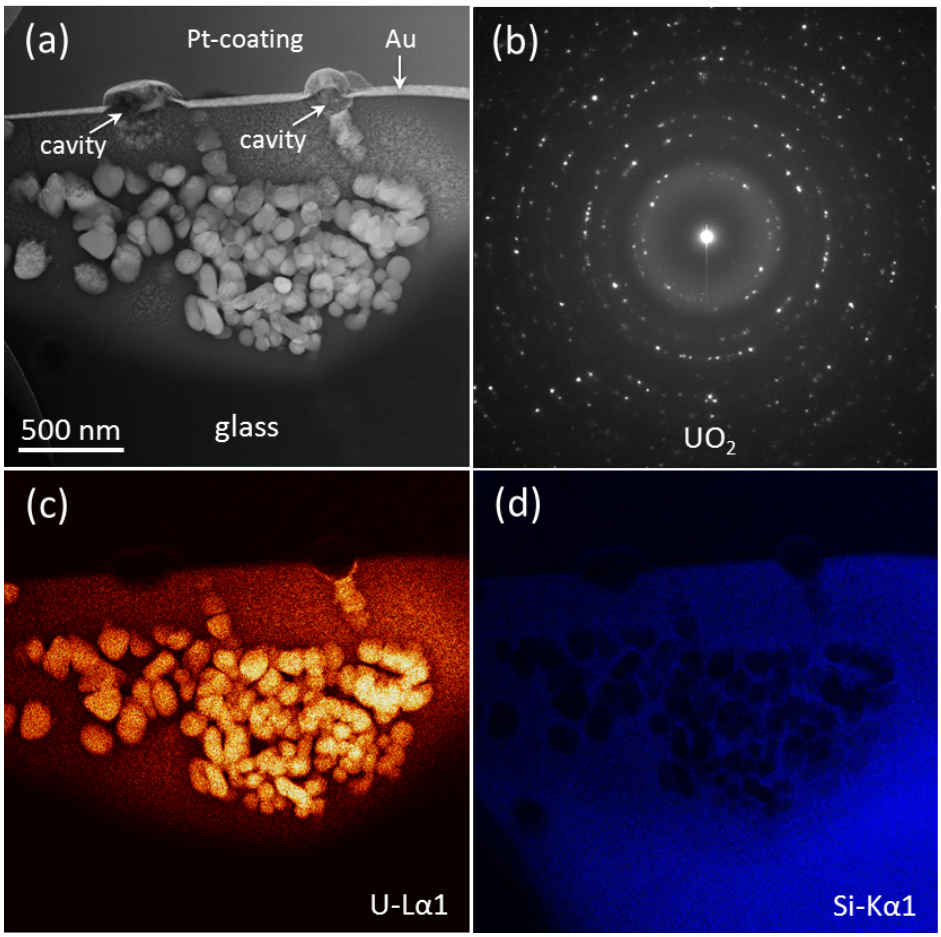

FIG. 10. (a) Z-contrast dark-field STEM image showing UO_2 nano-crystals embedded into the top glass plate from an area similar to that imaged in Fig. 7b. (b) Corresponding selected-area electron diffraction pattern indexed to be *fcc* UO_2. (c) & (d) X-ray EDS elemental maps of U-$L_{\alpha 1}$ and Si-$K_{\alpha 1}$, respectively, over area (a).

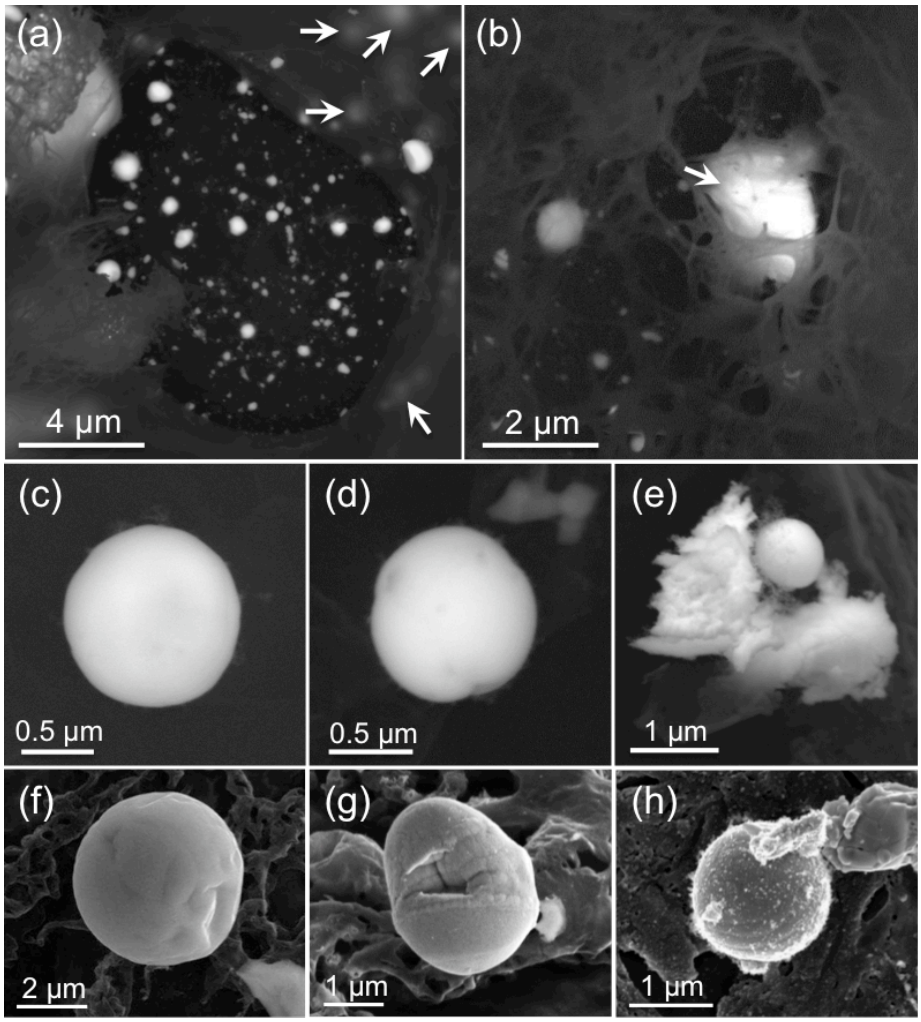

FIG. 11. (a) & (b) Low magnification backscattered electron SEM images showing the Kapton film (dark contrast) and recovered materials (lighter contrast) after an arc. (c)-(e) Backscattered electron SEM images of some typical uranium-containing spherules and debris. (f), (g) & (h) Secondary electron SEM images of typical uranium-containing spherules, referred to as S-1 (f), S-2 (g) and S-3 (h), respectively, and detailed further in Figures 12, 13 and 14.

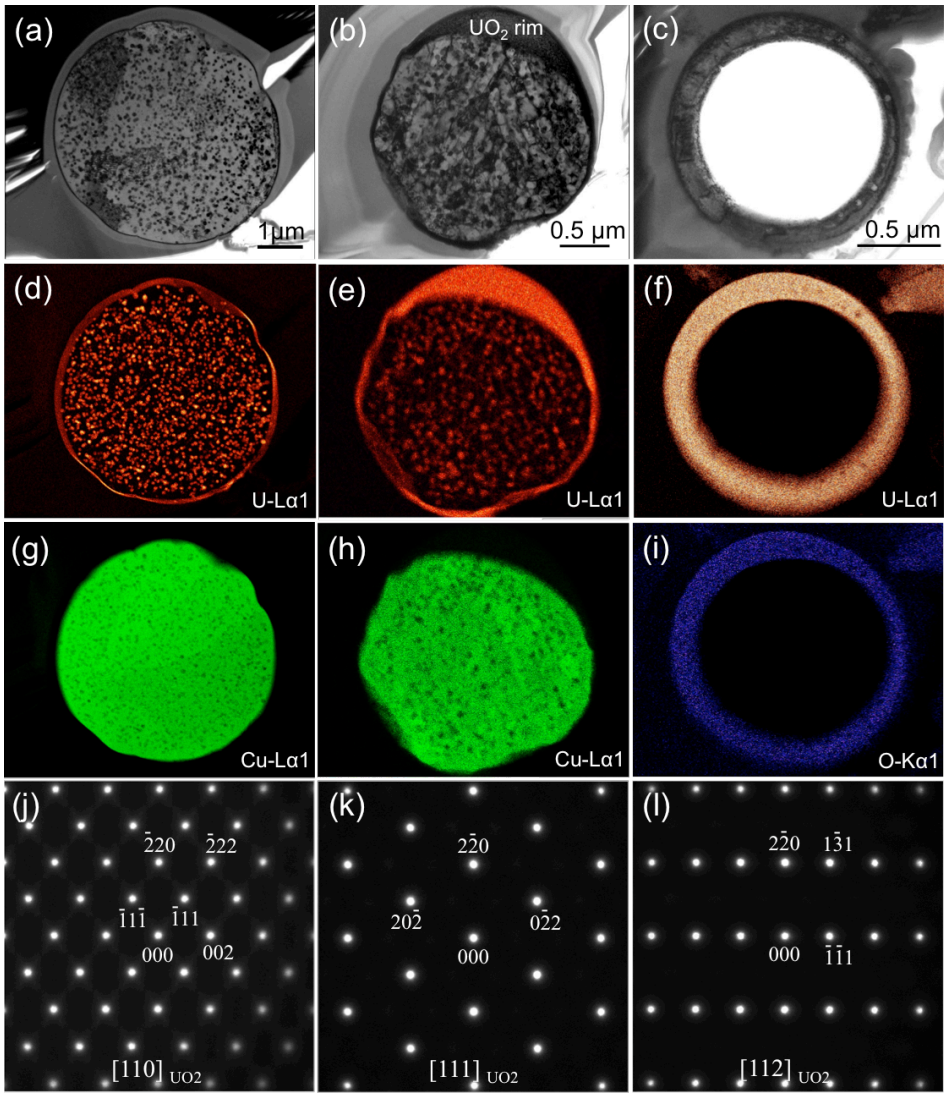

FIG. 12. Bright-field TEM images of cross-sections of the spherules: S-1 (a), S-2 (b) and S-3 (c). X-ray elemental maps of U-$L_{\alpha 1}$ for the spherules: S-1 (d), S-2 (e) and S-3 (f). X-ray elemental maps of Cu-$K_{\alpha 1}$ for the spherules: S-1 (g) and S-2 (h). X-ray elemental maps of O-$K_{\alpha 1}$ for the spherule S-3 (i). (j)-(l) Selected-area electron diffraction patterns taken from the UO_2 rim of S-2 (b).

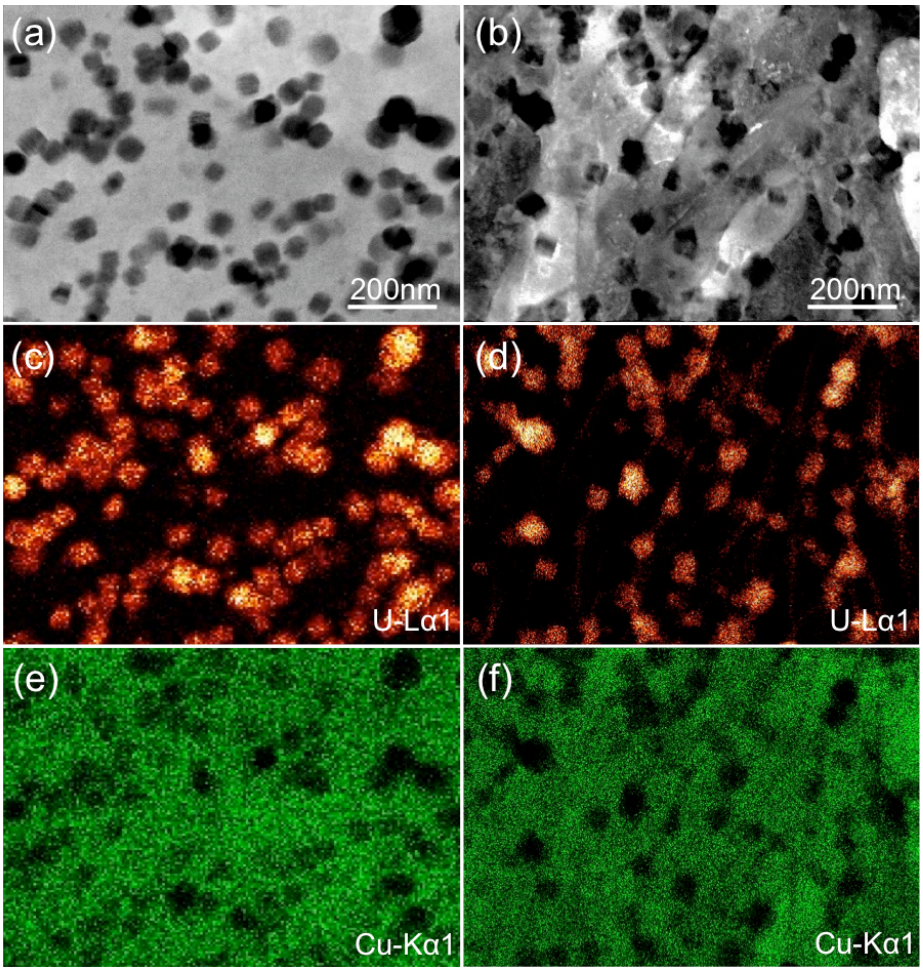

FIG. 13. Enlarged bright-field TEM images of the uranium-containing spherules S-1 (a) and S-2 (b). (c)-(d) and (e)-(f) Corresponding X-ray EDS elemental maps of U-$L_{\alpha 1}$ and Cu-$K_{\alpha 1}$, respectively.

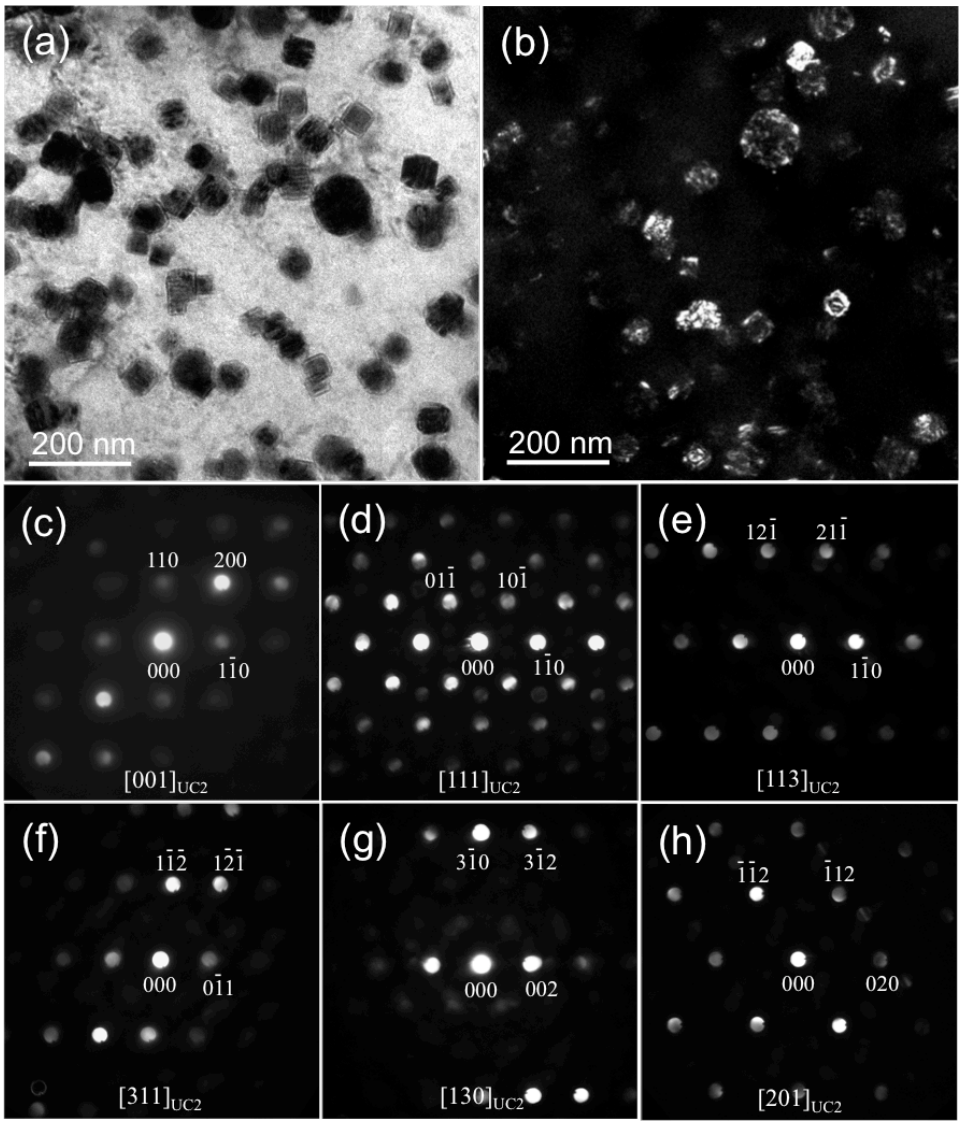

FIG. 14. Enlarged bright-field (a) and dark-field (b) TEM images of recovered spherule S-1. (c)-(h) A series of electron microdiffraction patterns taken from individual included UC_2 nanocrystals embedded in the S-1 spherule (Fig. 12a).